The Lifetimes of Plasma Structures at High Latitudes

Magnus F Ivarsen[1], Yaqi Jin[1], Andres Spicher[1], Wojciech Miloch[1], and Lasse B N Clausen[1]

[1]Department of Physics, University of Oslo, Oslo, Norway

Key Points:

- The ratio of E-region to F-region conductance is an accurate predictor of F-region polar cap plasma diffusion.
- The observed scale-dependency of the structure lifetimes deviates strongly from the theoretical predictions.
- F-region small-scale plasma structure lifetimes in the central polar caps range from 1 to 3 hours.

Corresponding author: Magnus F Ivarsen, m.f.ivarsen@fys.uio.no

Abstract
We present an investigation of polar cap plasma structure lifetimes. We analyze both simulated data from ionospheric models (International Reference Ionosphere model and Mass Spectrometer Incoherent Scatter model) and in-situ data from the Swarm satellite mission (the 16 Hz Advanced Plasma Density data set). We find that the theoretical prediction that E-region conductance is a predictor of F-region polar cap plasma structure lifetimes is indeed supported by both in-situ-based observations and by ionospheric models. In-situ plasma structure lifetimes correlate well with the ratio of F- to E-region conductance. We present explicit predictions of small scale (~ 1 km) structure lifetimes, which range from less than 1 hour during local summer to around 3 hours during local winter. We highlight a large discrepancy between the observational and theoretical scale-dependency of decay due to diffusion.

1 Introduction

In the high-latitude ionosphere, the primary source regions for plasma structuring tend to be located in the dayside cusp and the nightside auroral oval, where electron precipitation is abundant (Kelley et al., 1982). The large-scale polar convection pattern then causes the structured plasma to travel anti-sunward through the polar cap (Dungey, 1961; Cowley & Lockwood, 1992). In fact, the transport of irregularities from particle precipitation-driven source regions into the polar cap proper is an essential reason for the observed polar cap plasma structures (Cowley, 2000), although alternative sources of structuring inside the polar cap proper exist, such as the gradient drift instability mechanism (e.g., Tsunoda, 1988). Without an irregularity production source, the lifetime of a given plasma structure entering the polar cap is an indicator of the effectiveness with which the plasma structures are diffusing into the surrounding plasma. Indeed, Jin et al. (2017) found that occurrence of plasma irregularities drops significantly when plasma leaves the cusp region.

The occurrence of plasma irregularities in the high-latitude regions is in general subject to strong seasonal dependencies (Heppner et al., 1993; Ghezelbash et al., 2014; Prikryl et al., 2015; Jin et al., 2018). In general, local winter is accompanied by an increase in observed plasma irregularities. Additionally, the occurrence rate for the large-scale polar cap patches is higher during local winter (Foster, 1984; Schunk & Sojka, 1987; Coley & Heelis, 1998; Wood & Pryse, 2010; Spicher et al., 2017), though conflicting evidence exists for the southern hemisphere (Noja et al., 2013; Chartier et al., 2018). Recently, Ivarsen et al. (2019) found clear evidence for the seasonal dependency plasma structure diffusion, on average for scales < 5.8 km, concluding that local season is a powerful indicator for the existence of plasma irregularity dissipation.

Pressure gradients in plasma cause plasma density structures to diffuse into the surrounding plasma (Vickrey & Kelley, 1982). In radial structures, plasma distributed in a long column with an axial external magnetic field applied — assuming rotational symmetry — is only subject to radial, or perpendicular diffusion. Theoretically, in this plasma, ions and electrons diffuse individually (Moisan & Pelletier, 2012). This creates a charge-induced (ambipolar) electric field, which in turn serves to decelerate the diffusion of the faster-diffusing species, and accelerate the slower-diffusing species (Moisan & Pelletier, 2012). The value of the ambipolar electric field then controls the rate of diffusion of plasma structures in the F-region. In a seminal article, Vickrey and Kelley (1982) showed that, theoretically, the height-integrated ionospheric Pedersen conductivity controls the ambipolar electric field, and thus also the rate of F-region plasma diffusion. This mechanism gives rise to the observed seasonal dependency of plasma structure abundance. The equation expressing the height-integrated perpendicular diffusion coefficient in the F-region

polar cap reads (Vickrey & Kelley, 1982),

$$D_\perp = \frac{\Sigma_i^F}{\Sigma_i^F + \Sigma_e^F + \Sigma_i^E + \Sigma_e^E} \left(D_{\perp,e} - D_{\perp,i}\right) + D_{\perp,i}, \tag{1}$$

where Σ_j^k is the height-integrated Pedersen conductivity for the regions $k = E,\ F$, and $D_{\perp,j}$ is the height-integrated perpendicular diffusion coefficient, both for species $j = i,\ e$. In reality, the Pedersen current is primarily carried by ions, and so the height-integrated Pedersen conductivity can be defined in terms of the ion conductivity only, $\Sigma^k \approx \Sigma_i^k$.

With this simplification, it is now instructional to write Eq. (1) as,

$$D_\perp = \frac{\Sigma^F D_{\perp,e} + \Sigma^E D_{\perp,i}}{\Sigma^F + \Sigma^E}. \tag{2}$$

Since the diffusion coefficient of species j is proportional to mass of that species, $D_{\perp,i} \gg D_{\perp,e}$. Given that the ratio of E-region to F-region conductance is substantially greater than $D_{\perp,e}/D_{\perp,i}$ (an assumption that will be validated in the Results section), we can simplify further,

$$D_\perp = \frac{\Sigma^E}{\Sigma^F + \Sigma^E} D_{\perp,i}. \tag{3}$$

Physically, Eq. (1) illustrates that a strengthening of Pedersen conductivity in the E-region as opposed to the F-region shorts out the ambipolar electric field, causing F-region plasma to diffuse at the high ion perpendicular diffusion rate instead of the balanced ambipolar diffusion rate [the applied magnetic field causes ion rates to be much higher than the electron rates, the reverse of the situation without such a magnetic field (Moisan & Pelletier, 2012)]. As shown by Eq. (3), as long as the ratio of E-region to F-region conductance is not negligibly small, the electrons play no role in the perpendicular plasma diffusion considered here. The electrons are frozen in the magnetic field lines, while, as mentioned, the ions carry the Pedersen currents. Incident sunlight photo-ionization, which typically causes the E-region conductivity, and is thus the primary driver for fractional factor in Eq. (3), displays a strong seasonal dependence in the polar caps. This is the primary driver for observed seasonal dependencies in polar cap plasma irregularity dynamics (Basu et al., 1988; Kelley et al., 1982; Vickrey & Kelley, 1982; Kivanc & Heelis, 1998; Milan et al., 1999; Danskin et al., 2002; Jin et al., 2018).

Let us now turn to the subject of an observable quantity related to the perpendicular diffusion coefficient: structure lifetime. In general, the time scale associated with a diffusion process adheres to the following equation (Huba & Ossakow, 1981; Moisan & Pelletier, 2012),

$$\tau = \frac{\hat{\lambda}^2}{D}, \tag{4}$$

where $\hat{\lambda}$ is a characteristic scale length, and D is the mentioned diffusion coefficient. Plugging Eq. 3 into Eq. 4, we can express an estimate for F-region polar cap perpendicular plasma structure lifetimes $\tau_\perp$ as predicted by Vickrey and Kelley (1982),

$$\tau_\perp = \left(1 + \frac{\Sigma^F}{\Sigma^E}\right) \frac{\hat{\lambda}^2}{D_{\perp,i}}. \tag{5}$$

Note that small-scale high latitude F-region plasma structures are believed to be generated through instability processes and be the result of the balance between production and decay (Tsunoda, 1988). Consequently, the growth of plasma structures may also effectively increase τ in Eq. (4).

Unfortunately, the subject of plasma structure lifetime is rarely explicitly addressed. However, the lifetimes of polar cap patches has been documented in the literature. Due to chemical recombination, the density of polar cap patches decay towards the ambient plasma density (Wood & Pryse, 2010). Through the application of ionospheric modelling,

Schunk and Sojka (1987) likewise concluded that the lifetime of a typical polar cap patch during local summer is 4 hours, while during local winter the lifetime is 11 hours, with lifetime defined as a decay of a patch from 10 times the ambient plasma density to a density 10% higher than the ambient plasma. Using all-sky imager data, Hosokawa et al. (2011) calculated the decay time of polar cap patches due to chemical recombination, in a case study of an equinox patch. They concluded that the lifetime of the patch in question was highly altitude-dependent, with the shortest lifetime being 1 hour, at an altitude near the F-region peak of 250 km, where lifetime was defined as a reduction to $1/e$ times the original patch density.

The driving force behind polar cap patch decay, chemical recombination, is not dependent on plasma structure scale, and is a competing process to the ambipolar diffusion [Eq. (3)]. The dominant ion is O^+, and charge exchange collisions of O^+ with neutral species, which result in N_2^+ and O_2^+, are the main processes through which ions diffuse vertically (Johnsen & Biondi, 1980; Hosokawa et al., 2011). At altitudes above the F-region peak at around 250 km, ambipolar diffusion will be faster than the decay time due to chemical recombination, but the latter will impact plasma densities at the topside F-region through vertical diffusion. In the case of competing decay times τ_c (chemical) and $\tau_\perp$ (diffusion), the combined decay time should be given by,

$$\tau = \frac{\tau_c \tau_\perp}{\tau_c + \tau_\perp}. \tag{6}$$

The present study is a follow-up investigation based on the findings in Ivarsen et al. (2019). In the previous study, we found through an automatic detection of breakpoints in the PSD of Swarm 16 Hz plasma density observations in the polar caps, that around 80% of sampled local summer polar cap plasma exhibited direct evidence of plasma structure dissipation due to plasma diffusion. The corresponding fraction for the local winter polar caps were around 20%. We found that this seasonal dependency is highly predictable, and is tightly connected to solar zenith angle, which in turn controls the amount of EUV photoionization due to solar radiation. In the present study, we intend to investigate high-latitude plasma structure lifetimes. By applying both state of the art ionospheric models, and by using data from in-situ satellite missions, we find that the theoretical predictions put forth by Vickrey and Kelley (1982), namely that E-region conductance controls the F-region plasma structure lifetimes in the polar cap, is indeed supported by evidence.

2 Methodology

There are two aspects to the methodology developed in the present study. First, we make an estimate of plasma structure lifetimes in the polar caps based on in-situ data from the Swarm mission. Second, we approach the perpendicular diffusion coefficient using ionospheric plasma models.

2.1 In-situ plasma structure lifetime estimate

Ignoring irregularity production and chemical recombination, we can assume that a portion of plasma (e.g., a polar patch) is convecting anti-sunward through the polar cap, that it only undergoes diffusion, and that it diffuses at a constant rate. Our central assumption is then that a satellite orbiting through the F-region ionosphere plasma will, at any given point along the sun-midnight line, encounter plasma that has undergone convection with a constant velocity, and diffusion without further irregularity production.

Using high-resolution (16 Hz) in-situ plasma density from the Swarm mission (Friis-Christensen et al., 2006; Knudsen et al., 2017), we can estimate small-scale plasma structuring using the observed power spectral density of the measured electron density. With

a sampling frequency of 16 Hz, we can probe fluctuations for a range of scales down to about 1 km, assuming that the plasma velocity is much smaller than the satellite velocity. At high latitudes, Swarm orbit will be almost perpendicular to Earth's magnetic field lines, and so an orbiting satellite will sample plasma structures perpendicular to the ambient magnetic field.

We consider all polar cap passes between noon and midnight made by Swarm A between 15 October 2014 and 1 July 2019, at an altitude of approximately 460 km. We use data from Swarm A in this study, but the following analysis can be applied to data from each of the three Swarm satellites with similar results. For each overpass, we translate Swarm A travel time to the distance along a straight line connecting noon to midnight,

$$d = (t - t_0) v_S \cos\alpha, \tag{7}$$

where d is the distance travelled by the convecting plasma, v_S is the orbital velocity of Swarm A, α is the angle made by the orbit with respect to the noon-midnight line, t is Swarm A time, and t_0 is the time at which Swarm A approaches the polar cap. We consider polar cap passes where $\alpha < 30°$, and where the satellite is located poleward of $\pm 82°$ at some point during the pass.

Next, we analyze the measured electron density n. In order to look at fluctuations irrespective of the background density, we consider the unitless relative density perturbations,

$$\tilde{n} = \frac{n - \bar{n}_{1m}}{\bar{n}_{1m}}, \tag{8}$$

where n_{1m} is a running median filter with a window size of 1 minute. We perform a power spectral density analysis (PSD) on $\tilde{n}$. Here, we use a variant of Welch's PSD method, which consists of averaging modified periodograms over a logarithmically spaced spectral range (Welch, 1967; Trbs & Heinzel, 2006). We use an overlapping bin size of 60 seconds, with a temporal resolution of 1 second. For each bin, we integrate the PSD over 29 logarithmically spaced intervals, from 0.015 Hz down to the Nyquist frequency at 8 Hz. The integral of the PSD, given a stationary process, corresponds to the root-mean-square (RMS), the square root of which is referred to as the standard deviation, σ. We define the scale-dependent σ_λ as,

$$\sigma_\lambda = \sqrt{\int_{\Delta\lambda} S(\omega)\, d\omega}, \tag{9}$$

where $S(\omega)$ is the PSD, ω being the frequency, and λ is the midpoint of the scale interval $\Delta\lambda$. The integral is performed over the frequency interval $\Delta\lambda$, where,

$$\Delta\lambda = \frac{v_S}{\Delta\omega}, \tag{10}$$

assuming that the plasma velocity is much smaller than the Swarm orbital velocity v_S. In this framework, σ_λ represents the strength of fluctuations in the plasma density at the scale λ. Some density fluctuation powerspectra made using Swarm 16 Hz plasma density exhibit noise in the highest frequencies (Ivarsen et al., 2019). As a precaution, we impose upon the computed RMS values the requirement that, $\sigma_\lambda > 6{\times}10^{-4}$, a threshold found after extensive testing.

Following from the assumptions laid down so far, plasma containing fluctuations characterized by σ_λ will, once it enters the polar cap, diffuse at a constant rate $D_\perp$. The time evolution of a diffusion process on σ_λ with the time scale τ_S is characterized by the following differential equation (e.g., Moisan & Pelletier, 2012),

$$\frac{\mathrm{d}\sigma_\lambda}{\mathrm{d}t_c} = -\frac{1}{\tau_S}\sigma_\lambda, \tag{11}$$

which has the solution,

$$\sigma_\lambda(t_c) = \sigma_\lambda(0)\ \exp\left(-\frac{t_c}{\tau_S}\right). \tag{12}$$

In Eqs. (11) and (12), t_c is the plasma convection time and $\sigma_\lambda(0)$ is the initial RMS value at the point of entry into the polar cap. Now, to convert Swarm orbital distance d along the noon-midnight line (Eq. 7) to plasma convection time, we write $t_c = d/v_c$, with v_c being the plasma convection velocity. In combination with Eq. (7), we then have for the plasma convection time,

$$t_c = \frac{v_S}{v_c}(t - t_0)\cos\alpha. \tag{13}$$

For each Swarm A orbit between noon and midnight, we store the plasma convection time t_c and the relative density fluctuations σ_λ for all 29 frequency intervals.

Note that we use τ_S to distinguish the structure lifetime from the theoretical decay time τ — as we expect that structure lifetime as estimated in the present study will deviate from the theoretical decay time. Nevertheless, we can apply Eq. (5) to express the theoretically predicted structure lifetimes. As dictated by the Fourier analysis we apply, the density gradients are associated with a wavevector $k_\perp = 2\pi/\lambda$, meaning that the scale $\hat{\lambda}$ in Eq. (5) is in fact λ divided by 2π,

$$\hat{\lambda} = \frac{\lambda}{2\pi}, \tag{14}$$

and so,

$$\tau_\perp = \left(1 + \frac{\Sigma^F}{\Sigma^E}\right)\frac{\lambda^2}{4\pi^2 D_{i,\perp}}. \tag{15}$$

With the assumption that the convecting structures treated in the present section only undergo perpendicular diffusion, τ_S in Eq. (12) will approach $\tau_\perp$ in Eq. (15).

The precise location of the cusp is known to vary both in magnetic latitude (MLAT) and magnetic local time (MLT), based on conditions related to the ionosphere-magnetosphere connection and the orientation of the interplanetary magnetic field (IMF). On average, the cusp tends to be located at around $\pm 75°$ MLAT, and slightly towards the pre-noon sector (Lotko et al., 2014; Jin et al., 2019). Though varying, with the methodology outlined here, Swarm A will nevertheless on average orbit through the cusp, given that we analyze a large number of orbits.

2.2 Modelling the effective perpendicular diffusion coefficient

Our goal is to evaluate Eq. (1). To this end, we need expressions for the field-perpendicular diffusion coefficients and the Pedersen conductivity height profiles, both of which depend on the collision frequencies between the plasma species. First, we use expressions from Moisan and Pelletier (2012) for collisional plasma interactions ($d_{\perp,j}$ and $\sigma_{\perp,j}$), which are given below. Second, we use values for the collision interaction terms between all charged particles associated with the ion species in the ionosphere, as presented in Schunk and Nagy (1980). Third, we use the International Reference Ionosphere model (IRI) for the ionospheric ion species number densities and plasma temperatures (Bilitza & Reinisch, 2008; Bilitza et al., 2014), the Mass Spectrometer Incoherent Scatter model (MSIS) for the neutral number densities (Picone et al., 2002), and IGRF for the magnetic field strength (Thbault et al., 2015). These models are not meant to offer accurate descriptions of highly localized phenomena such as the cusp, which is sensitive to the ionosphere-magnetosphere coupling. We nevertheless find that when aggregated, the simulated data offer insight into the relationship between E- and F-region conductances.

The field-perpendicular diffusion coefficient (not height-integrated) from charged particle collisions is defined as (Moisan & Pelletier, 2012),

$$d_{\perp,j} = \frac{d_{0,j}\nu_j^2}{\omega_j^2 + \nu_j^2}, \tag{16}$$

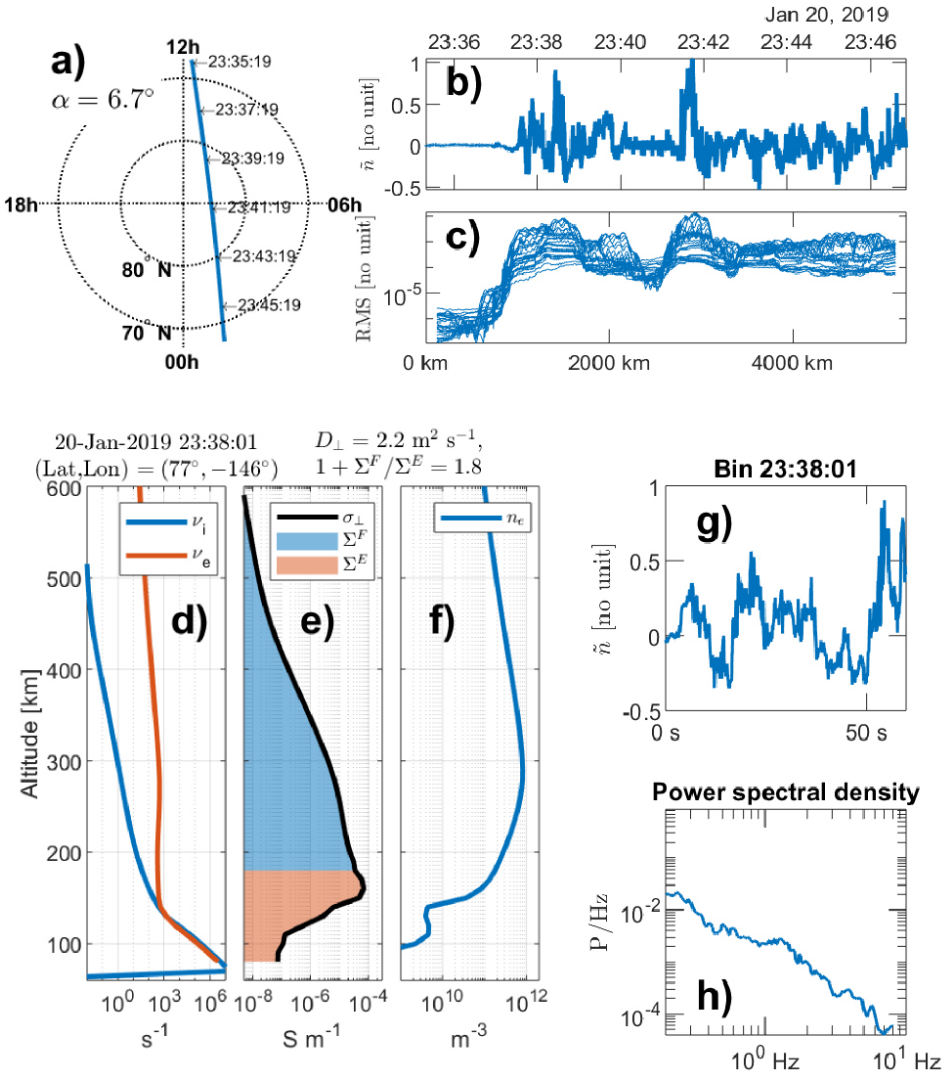

Figure 1. Example of the data analysis performed on the Swarm 16 Hz plasma density data. In panel a), we show Swarm A orbit across the northern polar cap during a 10 minute interval, with α, the angle of the orbit against the noon-midnight line, indicated. The orbit in panel a) is shown in an MLAT-MLT coordinate system. In panel b), the 16 Hz relative electron density perturbations for a 12-minute polar cap pass is displayed, showing the cusp encountered around 23:38:00 UT, and in panel c) we show the RMS data plotted against the plasma convection distance d (Eq. 7). The RMS timeseries consists of the integrated PSD over 29 frequency intervals, with a running 1-minute window, and a resolution of 1 second. In the lower panels we show the specific analysis of a point in time centered on 20 January 2019, 23:38:01 UT. Panel d) shows the collision frequencies (calculated using values of the interaction terms from Schunk and Nagy (1980) and MSIS), and panel e) shows the resulting Pedersen conductivity height profiles, with the values of $D_\perp$ and $1 + \Sigma^F/\Sigma^E$ indicated above the plot. Panel f) shows the electron density altitude profile. Panel g) shows the 1-minute relative density perturbation segment centered on 23:38:01 UT, while panel h) shows the PSD based on this segment.

where, $d_{0,j} = k_B T_j / m_j \nu_j$, with k_B the Boltzmann constant, T_j the temperature, $\omega_j = eB/m_j$ the cyclotron frequency, and m_j is particle mass, all for species j. ν_j is the composite collision frequency,

$$\nu_i = \nu_{in}, \tag{17}$$

$$\nu_e = \nu_{en} + \nu_{ei}, \tag{18}$$

where subscripts i, e, n denote ions, electrons, and neutrals respectively.

The ionospheric Pedersen conductivity is given by (Moisan & Pelletier, 2012),

$$\sigma_{\perp,j} = \frac{e^2 n_j}{m_j} \frac{\nu_j}{\omega_j^2 + \nu_j^2} \tag{19}$$

where m_j and n_j is the effective mass and number density for species j respectively.

Next, we need expressions for the height-integrations of Eqs. (16) and (19). The height-integrated perpendicular diffusion coefficient $D_{\perp,j}$ is defined as (Vickrey & Kelley, 1982),

$$D_{\perp,j} = \frac{1}{N} \int_{z0}^{\infty} dz \; n_e(z) d_{\perp,j}(z), \tag{20}$$

for species j, and where z signifies the altitude dependency. z_0 is the lowest altitude of the F-region, and N is the height-integrated plasma density, $N = \int_{z_0}^{\infty} dz \; n_e(z)$. Furthermore, the height integrated Pedersen conductivity, or conductance, $\Sigma_j^{E,F}$, is defined as (Vickrey & Kelley, 1982),

$$\Sigma_j^k = \int_k dz \; \sigma_{\perp,j}(z), \tag{21}$$

for species j, and where $k = E, F$ signifies the region, and $\sigma_{\perp,j}(z)$ is the altitude dependent ionospheric Pedersen conductivity (Eq. 19).

Now we are in a position to evaluate Eq. (1). First, we compute the Pedersen conductivity (Eq. 19) for altitudes from 60 km to 600 km, with a 10 km interval. Second, we integrate the resulting height profiles, in addition to the electron density height profiles (from MSIS), and evaluate Eq. (20). Third, using the height-integrals in Eqs. (19, 20), we evaluate Eq. (1). For each polar cap pass made by Swarm A, we then calculate and store the values of $1 + \Sigma^F / \Sigma^E$ and $D_\perp$ on a time grid covering the pass.

Fig. 1 documents the data analysis applied to the Swarm 16 Hz plasma density data, along with the application of ionospheric models. Panels a), b) and c) show an entire example polar cap pass, where the orbit, along with the value of α, is shown in panel a), the relative density fluctuation (Eq. 8) is shown in panel b), and the 29 RMS timeseries resulting from integrating the PSD over a running 1-minute window are shown in panel c). An example 1-minute segment of the relative density perturbations, and the corresponding PSD, are shown in panels f) and g). Panels d) and e) show height-profiles of the collision frequencies (Eqs. 17, 18), and the Pedersen conductivity (Eq. 19), with the values of $1 + \Sigma^F / \Sigma^E$ and $D_\perp$ indicated.

3 Results

We perform a superposed epoch analysis on the Swarm A polar cap passes. To distinguish between different seasons, we use a 131-day window centered on the December and June solstices, without specifying the year of the polar cap pass. During the period between 14 October 2014 and 30 June 2019, we registered a total of 3366 passes in the northern hemisphere, and 1698 passes in the southern hemisphere. The reason for the large number discrepancy is due to Swarm orbital dynamics: the polar orbit of Swarm

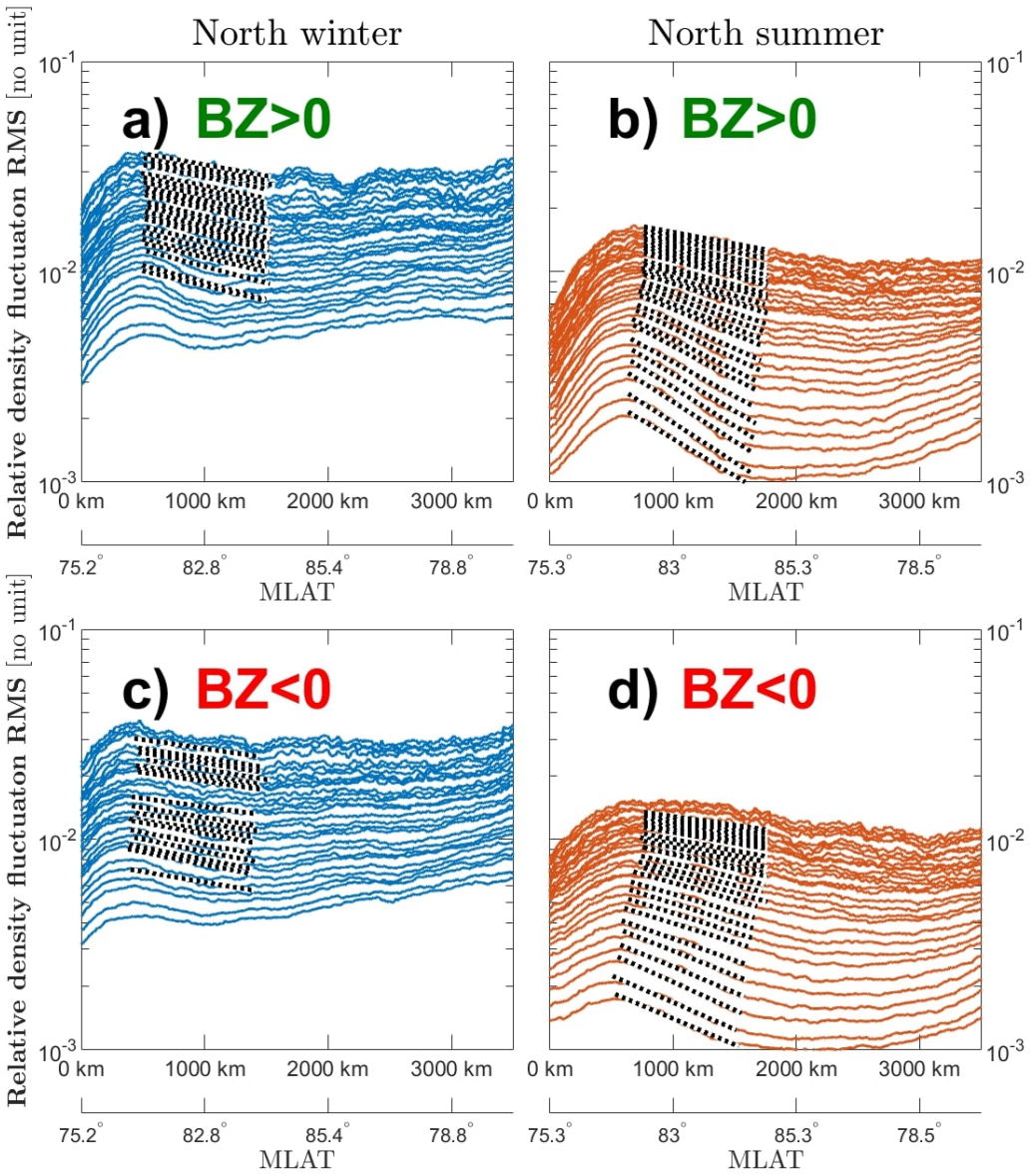

Figure 2. Plasma structure decay time estimates based on 16 Hz plasma density data from the Swarm A satellite. The left panels show the superposed epoch analysis for 506 (a) and 550 (c) local winter passes, and the right panels show the superposed epoch analysis for 647 (b) and 598 (d) local summer passes, through the northern polar cap. Both seasons are defined by a 131-day window centered on the relevant solstice. The curves for 29 frequency intervals are shown. The top panels (a and b) show passes made during northward IMF ($B_z > 0$), while the bottom panels (c and d) show passes made during southward IMF ($B_z < 0$). An exponential fit through 600 km of the assumed convection path of plasma through the polar cap is shown with dotted black lines (Eq. 12). The x-axes show both the underlying data MLAT, and the plasma convection distance (Eq. 7). The data used spans a time period from 2 Oct 2014 until 30 June 2019.

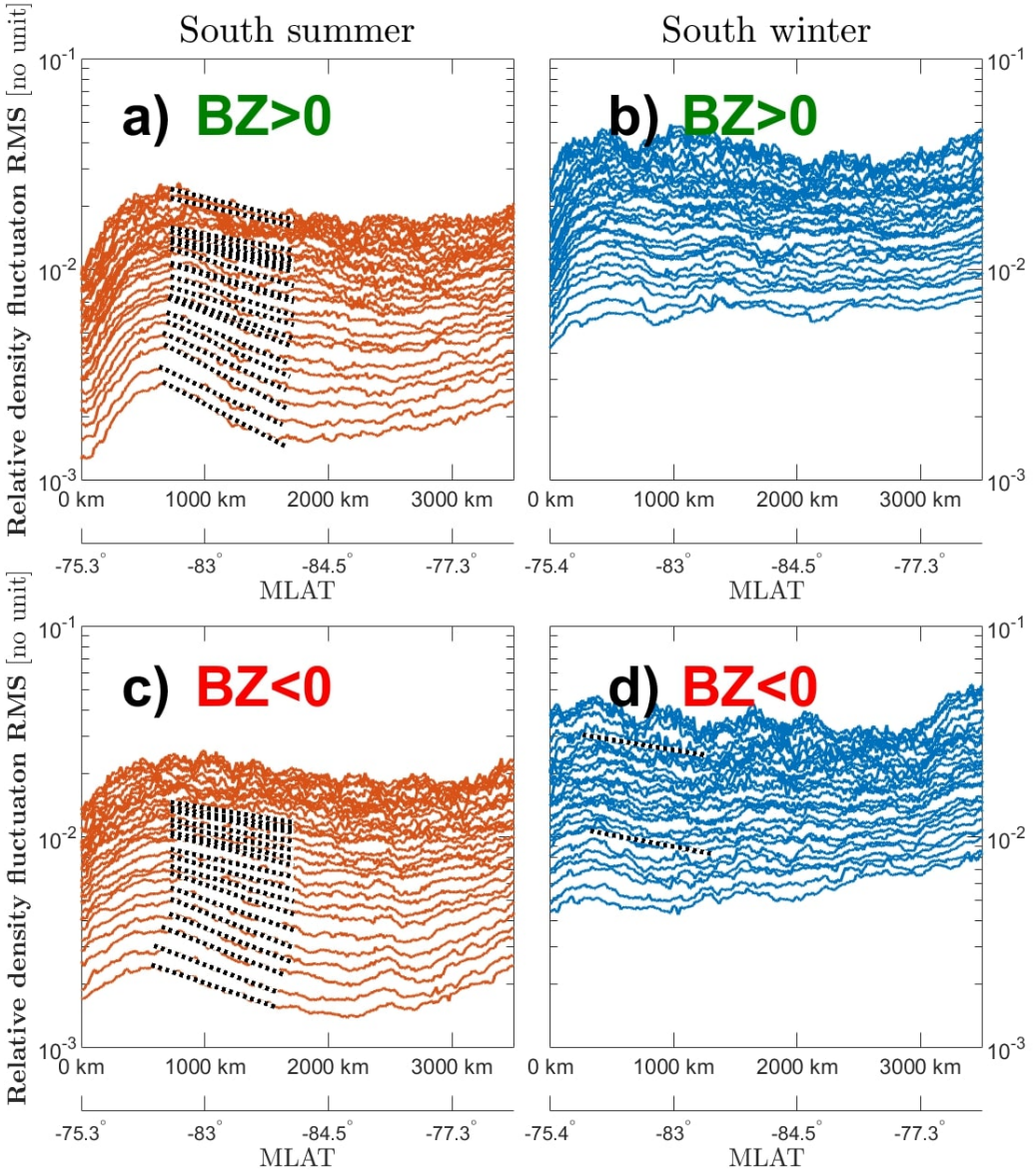

Figure 3. Equivalent to Fig. 2. The left panels show the superposed epoch analysis for 153 (a) and 185 (c) local winter passes, and the right panels show the superposed epoch analysis for 173 (b) and 159 (d) local summer passes, through the southern polar cap.

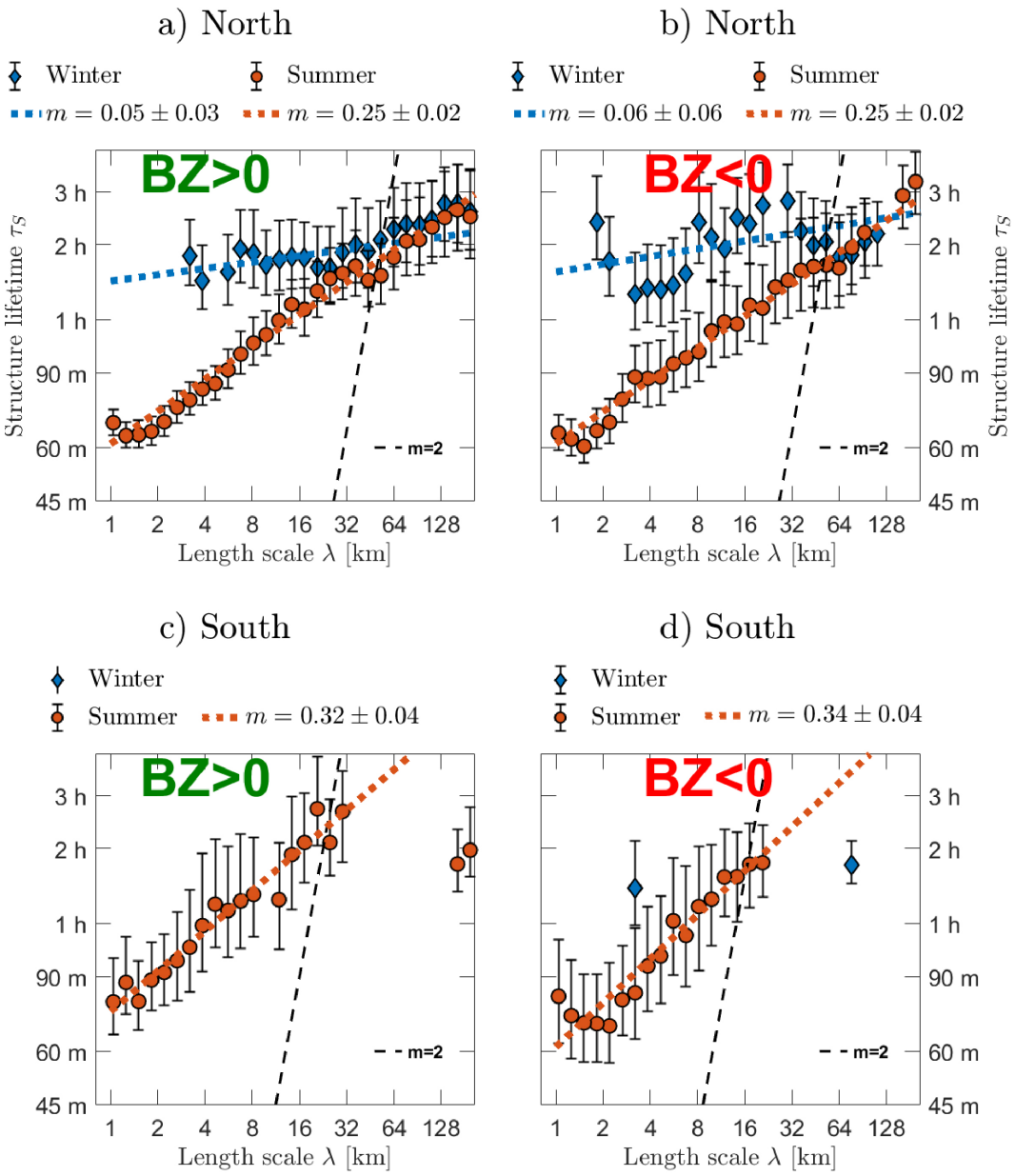

Figure 4. The scaling of the structure lifetime estimates, for local summer (orange) and local winter (blue), for both the northern (panels a and b) and southern (panel c and d) hemispheres. The left panels (a and c) show passes made during northward IMF ($B_z > 0$), while the right panels (b and d) show passes made during southward IMF ($B_z < 0$). The structure lifetimes, shown on the y-axes, correspond to the exponential fits displayed in Fig. 2. The vertical error-bars are the result of a Bootstrap error analysis (see text). Fits of Eq. (22) are shown in orange dotted lines, and the exponent m is indicated above (with error intervals corresponding to 90% confidence intervals of the fitting procedures). For illustration purposes, a fit of Eq. (22) with exponent $m = 2$ is shown in dashed black lines in each panel.

A is inclined 2.6 degrees from Earth's geographic axis. Compared to the northern hemisphere, the geomagnetic south pole is further away from the geographic south pole, leading to fewer noon-midnight passes occurring in the southern polar cap. Additionally, we make a distinction between passes occurring during southward and northward orientation of the IMF. That is, we distinguish between a polar cap-crossing average value of $B_z > 0$ and $B_z < 0$, B_z being the z component of the IMF, where we use observations from the bow shock, time shifted by around 15 minutes, as provided by OMNI (King & Papitashvili, 2005). Whether B_z is positive or negative is known to have an impact on polar cap plasma convection (Grocott et al., 2004), and a negative B_z in particular is associated with stronger ionospheric plasma irregularities (Cowley & Lockwood, 1992; Kivanc & Heelis, 1998). We found that sorting by the value of B_y had minimal impact on the results.

In Fig. 2, we show the result of the superposed epoch analysis for the northern hemisphere, for local winter (panels a and c) and local summer (panels b and d), and for B_z positive (panels a and b) and negative (panels c and d). The equivalent is shown in Fig. 3 for the southern hemisphere. Each panel shows the superposed values of σ_λ for the 29 frequency intervals considered, with distance (Eq. 7) and magnetic latitude on the x-axis. In all four panels, a prominent peak exists near the cusp regions, for all frequency intervals. This peak is located between 200 and 500 km after the average location of the cusp ($\pm 75^\circ$ MLAT). The reason for this increase might be related to the time it takes for precipitation events to be felt at the altitude of Swarm A (460 km), and the plasma structures might be undergoing growth rather than decay.

To estimate structure lifetime as outlined in the Methodology section, we fit Eq. (12) to each superposed σ_λ curve. That is, we fit an exponential curve through the polar cap, starting from a point after the peak near the cusp region, extending 1000 km into the central polar cap. Here, we assume a plasma convection velocity of 300 m/s for northward IMF, and 450 m/s for southward IMF, to account for the effect of IMF B_Z orientation on polar cap flow patterns (Reiff & Burch, 1985), reasonable velocities for the central polar cap (Grant et al., 1995; Thomas et al., 2015). Although this estimate might not be valid at all times, and at different locations in the polar cap, the fairly long distance over which we fit Eq. (12), 1000 km, will serve to average out spatial and temporal variations in flow velocity. Cases where the coefficient of determination, or r^2, of the fit is less than 0.8 are discarded, which stops virtually all the structure lifetimes from being evaluated in the southern hemisphere winter, where the superposed epoch analysis yields noisy curves. The characteristic time scale, τ_S, of the exponential fit reflects the expected structure lifetime of the fluctuations over the frequency interval in question, and is then the end-product of the superposed epoch analysis.

In Fig. 4, for the northern (panels a and b) and southern (panels c and d) hemispheres, we plot the structure lifetimes τ_S against the scale length λ at which the lifetime estimate was calculated. Panels a) and c) show passes where average values of B_z were positive, while panels b) and d) show passes where B_z on average was negative. λ is calculated based on the assumption that the plasma convection velocity is negligible compared to the velocity of Swarm A [Eq. (10)]. Local winter structure times are shown in blue, while local summer is shown in orange. The vertical errorbars are constructed from a Bootstrap routine. That is, we performed 5000 iterations of the analysis on a resampled dataset, where we sampled the entire dataset uniformly at random, with replacement. This provides 5000 individual estimates of each calculated quantity. The errorbars then represent 90-percent confidence intervals for the respective quantity, and represents a statistical uncertainty.

We see that while the local summer structure times for the most part monotonically increase with increasing length scale λ, the local winter structure times do not. The very smallest scales additionally do not monotonically increase with increasing length

scale. Also shown, in a dotted lines, is what amounts to a fit of Eq. (4). Here, we fit,

$$\tau_S = \tau_0 \left(\frac{\lambda}{\lambda_0}\right)^m, \tag{22}$$

where τ_0 and m are fitting parameters determined using linear regression, and λ_0 is a length scale equal to unity to ensure correct dimensionality in Eq. (22). The values of the exponent m are given in the four panels of Fig. 4, with error intervals given by the 90-percent confidence interval of the fitting procedure. We now make an important observation: the values of the exponent m reported here are far from the $m = 2$ in Eq. (4). Since the scaling difference between λ of Eq. (4) and λ of Eq. (22) will not affect the exponent m, the reported discrepancy is an unexpected result.

We see that the smallest scale, which corresponds to frequencies between 6.6 Hz and 8 Hz and has a scale length of 1 km, exhibits the largest seasonal contrast. To better understand this contrast, we construct a variable we refer to as wrapped day-of-year, D_w,

$$D_w = \begin{cases} 365 - D & \text{if } D > 365/2 \\ D & \text{otherwise,} \end{cases} \tag{23}$$

where D is the number of days elapsed since 1 January in the relevant year (day of year). We then make 9 overlapping bins with a window size of 65.5 days, from $D_w = [0, 65.5]$ to $D_w = [117, 182.5]$. For each bin, we repeat the superposed epoch analysis detailed above. Motivated by Eq. (15), which shows that the theoretical value of τ_S should be proportional to $1 + \Sigma^F/\Sigma^E$, we calculate Eq. (21) for points during the polar cap pass between $\pm 78°$ and $\pm 90°$ magnetic latitude. Then, for each D_w-bin we are left with an average value of $1 + \Sigma^F/\Sigma^E$.

To make a general prediction of 1 km-structure lifetimes in the polar cap, we calculate $D_\perp$ (Eq. 1), using the procedure outlined in the Methodology section. To gather a consistent picture of the polar caps, we evaluate Eq. (1) systematically for a geographic grid consisting of evenly spaced points poleward of $\pm 77°$ magnetic latitude, for 1400 points in time distributed throughout the years of 2015 throughout 2018, roughly equivalent to the time period covered by the Swarm data used in the present study. All the resulting values of $1 + \Sigma^F/\Sigma^E$ and $D_\perp$ for each snapshot of the polar cap are then aggregated — a total of 154,000 (for the northern hemisphere) and 145,000 (for the southern hemisphere) simulated data points are aggregated this way. We find that the lowest ratio of E- to F-region conductance in this dataset is around 0.1, validating the assumptions leading to Eq. (3).

To make a comparison with the structure lifetime estimates, we use Eq. (4), with $\hat{\lambda} = 2\pi/k_{1\text{km}}$, to express the theoretical decay time of 1 km-scaled structures,

$$\tau_{1\text{km}} = \frac{1}{k_{1\text{km}}^2 D_\perp}, \tag{24}$$

where $D_\perp$ is the model-based field-perpendicular diffusion coefficient (Eq. 1).

In panels a) (northern hemisphere) and b) (southern hemisphere) of Fig. 5, we show the result of this joint analysis: In color coded 2D-histograms, we show the distribution of model-based $D_\perp$ on the right y-axis, with the corresponding decay time (Eq. 24) on the left y-axis, and the value of $1 + \Sigma^F/\Sigma^E$ on the x-axis, in a log-log representation. The color scale refers to number of datapoints per pixel. In yellow circle markers ($B_z > 0$) and green triangle markers ($B_z < 0$), we show the in-situ estimated 1 km-structure lifetimes for 9 bins between December and June solstice, with the calculated value of $1 + \Sigma^F/\Sigma^E$ for each bin along the x-axis. The errorbars along the x-axis are the lower and upper quartile distributions of $1 + \Sigma^F/\Sigma^E$ in each bin, while the errorbars along the y-axis are 90-percent confidence intervals from the Bootstrap error analysis described above,

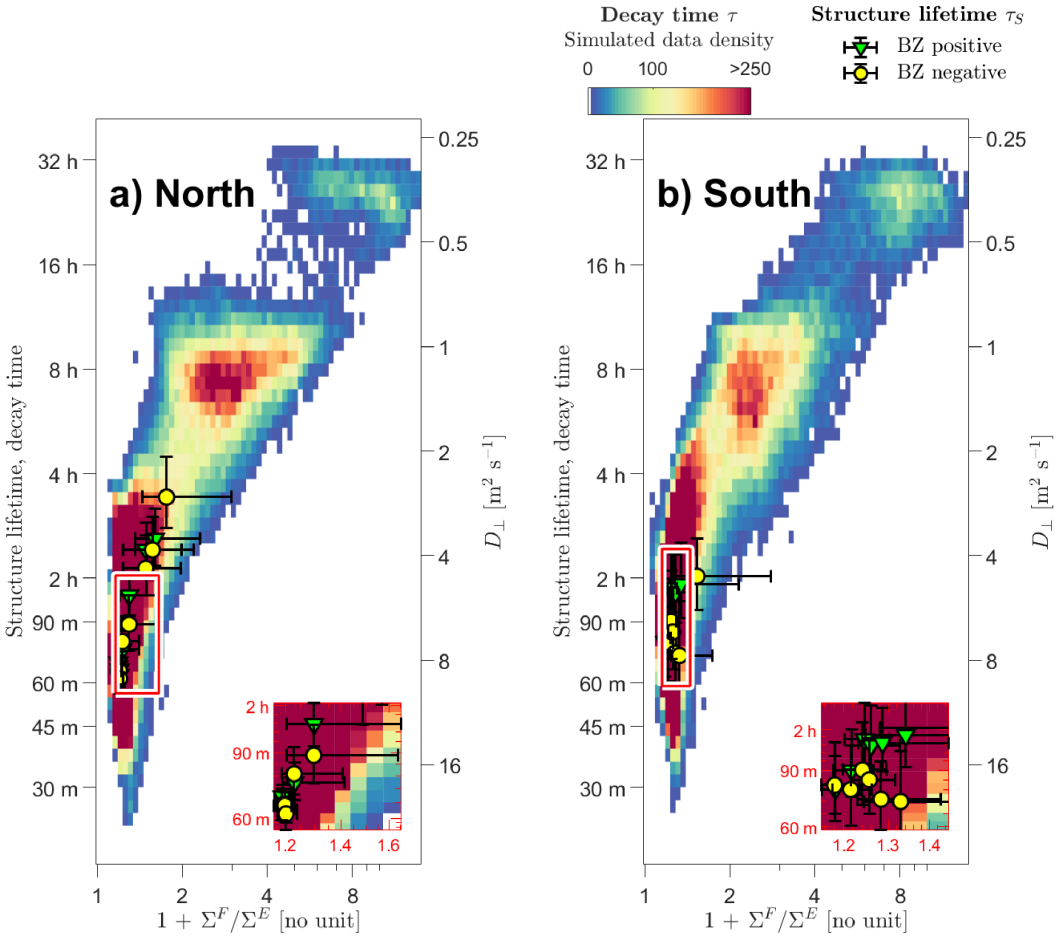

Figure 5. Color coded 2D-histograms show the distribution of the model-based $D_\perp$ on the right y-axis. On the left y-axis, we show the corresponding decay time (Eq. 24), and on the x-axis, the value of $1 + \Sigma^F/\Sigma^E$, for the northern hemisphere (panel a) and the southern hemisphere (panel b) . The color scale refers to number of datapoints per pixel. In yellow circle markers ($B_z > 0$) and green triangle markers ($B_z < 0$), the in-situ estimated 1 km-structure lifetimes for 9 bins between December and June solstice. The errorbars along the x-axis are the lower and upper quartile distributions of $1 + \Sigma^F/\Sigma^E$ in each bin, while the errorbars along the y-axis are 90-percent confidence intervals from the Bootstrap error analysis described above, performed on each D_w bin individually. Inset plots expand a tightly clustered rectangle indicated in both panels. All axes are in a $\log_{10}$ representation. The in-situ data covers the period from 14 October 2014 until 30 June 2019, while the model-based simulated data covers the years from 2015 through 2018.

performed on each D_w bin individually. An inset in the lower right corner of both panels expand a tightly clustered portion indicated by a red rectangle. The in-situ based τ_S estimates correlate well with the corresponding model-based $1 + \Sigma^F/\Sigma^E$-number, with a Pearson correlation coefficient of 0.99 ($B_z > 0$) and 0.97 ($B_z < 0$) for the northern hemisphere, and 0.86 ($B_z > 0$) and 0.70 ($B_z < 0$) for the southern hemisphere.

4 Discussion

In Fig. 4, we make the following significant observation: The estimated structure lifetime τ_S increases with structure scale for local summer, where a powerlaw with exponent around 1/4 accurately describes the scale-dependency of τ_S. The exponent deviates strongly from that of the theoretically predicted exponent of 2 [Eq. (4)]. As we shall now show, this result is wholly unexpected.

Chemical recombination of O_2^+ ions at the F-region peak will constitute a competing process to ambipolar diffusion by the decay of plasma density enhancements, and will impact plasma structures at Swarm altitude by vertical diffusion. The inverse of Eq. (6) implies that,

$$\frac{1}{\tau_S} = \frac{4\pi^2 D_\perp}{\lambda^2} + \frac{1}{\tau_c}, \tag{25}$$

where we use Eq. (4), again with $\hat{\lambda} = \lambda/2\pi$, to express $\tau_\perp$, and where we assume that the structure lifetime τ_S is a combination of diffusion and chemical decay times. Eq. (25) provides a possible explanation for the missing exponent $m = 2$ in Eq. (22); chemical recombination could form a plateau, where large-scale decay time due to diffusion would effectively be drowned out by the much faster scale-independent τ_c. However, no plateau is clearly visible for the large scales in Fig. 4, where the $m \approx 1/4$-fit describe the data with sufficient accuracy for all scales. As a solution to this apparent discrepancy, recall that we are analyzing the relative density fluctuations $\tilde{n}$, which are scaled by a 1-minute (460 km) average plasma density. Chemical recombination being scale-independent, n will decay at the same rate as $\bar{n}_{1m}$ [Eq. (8)], and so $\tilde{n}$ should be unaffected by chemical recombination.

Nevertheless, Eq. (25) opens up an opportunity, as a plot of reciprocal observed structure lifetimes $1/\tau_S$ against reciprocal scale squares $1/\lambda^2$ should reveal both the ambipolar diffusion coefficient $D_\perp$ and the constant chemical recombination decay time τ_c, from linear regression slope and intercept respectively. In Fig. 6 we show the result of the analysis presented in Section 2.1 applied to the absolute density fluctuations n, using the local summer data, for the northern (panels a and b) and southern (panels c and d) hemispheres, and for positive (panels a and c) and negative (panels b and d) IMF. Shown in black dotted lines, a fit of Eq. (25) reveals the calculated values of $D_\perp$ and τ_c, values of which are inset, with error margins given as 90% confidence intervals of the linear fits. Dashed blue lines show a fit of Eq. (22) for comparison. In all four panels a plateau can be inferred for scales roughly larger than 20 km, though for scales smaller than 8 km, the linear fit of Eq. (25) does not describe the data better than Eq. (22), indicating that the structure lifetimes under no circumstance scale with a theoretically predicted exponent of 2. However, if accepting the linear fit (black dashed lines) on face value, the ambipolar diffusion coefficient is valued between 3 and 7 $\mathrm{m^2 s^{-1}}$, and the chemical decay rate is valued between 2 and 3 hours. Though the ambipolar diffusion coefficient is in excellent agreement with the values shown in Fig. 5, we believe a more thorough exploration of the discrepancy between the exponents $m = 1/4$ in Eq. (22) and $m = 2$ in Eq. (4) should be prerequisite to interpreting the results in Fig. 6.

Looking at Figs. 2, 3, and 4, we now make the observation that the local winter structure times for the most part do not make the data correlation criteria, and thus allude the analysis, with the exception of the larger scales in the northern hemisphere. A possible explanation for this is that plasma diffusion during local winter is significantly

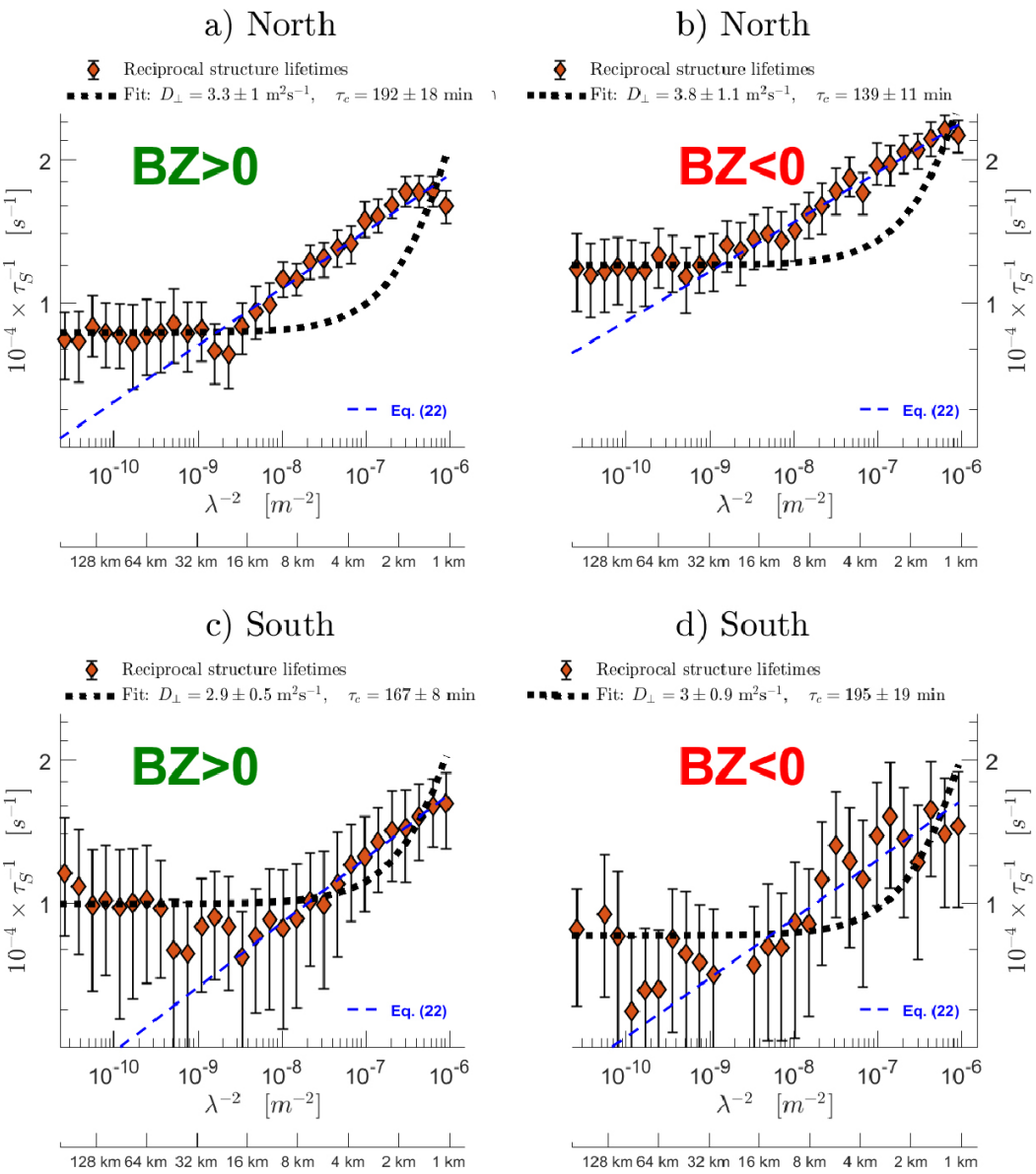

Figure 6. The result of the analysis presented in Section 2.1 applied to the absolute density fluctuations n instead of relative density fluctuations $\tilde{n}$, for the northern (panels a and b) and southern (panels c and d) hemispheres, and for positive (panels a and c) and negative (panels b and d) IMF. We show λ^{-2} along the upper x-axis and λ along the lower x-axis, and τ_S^{-1} along the y-axis. Orange diamonds are local summer structure lifetimes, with vertical errorbars the result of a 5000-iterations Bootstrap error analysis. The black dotted lines show a fit of Eq. (25), and the dashed blue lines show a fit of Eq. (22) fitted to the small-scale datapoint for comparison. The values of the parameters $D_\perp$ and τ_c are given above the plots, with error margins given by 90% confidence intervals from the fits.

reduced, which can explain the reported increase in local winter plasma irregularities (Heppner et al., 1993; Ghezelbash et al., 2014; Prikryl et al., 2015; Jin et al., 2017, 2018) In the previous study (Ivarsen et al., 2019, where we similarly analyzed 60-second segments of Swarm 16 Hz plasma density), we found that sampled local winter polar cap plasma tend not to show a signature of structure dissipation due to diffusion. In fact, only 20% of local winter plasma density segments exhibited evidence of plasma diffusion, while, conversely, 80% of local summer spectra did so. It is then not surprising that most ensemble averages of winter polar cap passes in the present study failed the stated data correlation requirement that the coefficient of determination be less than 0.8. Another factor that complicates local winter diffusion is the degree to which a conducting E-region shorts out the ambipolar electric field (Vickrey & Kelley, 1982). In the absence of a conducting E-region, anomalous currents could exist above the F-region, which could in turn lead to the existence of anomalous, or Bohm, diffusion in the F-region (Braginskii, 1965).

In Fig. 5, the model-based estimate for 1 km-decay times, $\tau_{1\text{km}}$ (Eq. 24), agree well with the in-situ-based structure lifetime estimates, τ_S (Eq. 12), for both hemispheres. However, the in-situ-based structure lifetimes are sensitive to the choice of plasma convection velocity, with higher velocities leading to a lowering of the value of τ_S. Nevertheless, the apparent *dependencies* visible in both $\tau_{1\text{km}}$ and τ_S of the $1 + \Sigma^F/\Sigma^E$-number show clear agreement: The in-situ-estimated structure lifetimes τ_S correlate well with the simultaneous model-based $1 + \Sigma^F/\Sigma^E$-number. They show correlation coefficients of up to 0.99 for the northern hemisphere, and up to 0.96 for the southern hemisphere. This is a strong indicator that the model first proposed by Vickrey and Kelley (1982) is suitable, and that the ratio of F-region to E-region conductance to a large degree predicts F-region diffusion rates, and thus the occurrence of plasma irregularities in the polar caps.

The reported agreement in how both the in-situ based structure time and the model-based decay time respond to the $1 + \Sigma^F/\Sigma^E$-number is largely only valid for the smallest scales available to investigation using the Swarm 16 Hz plasma density data, after which the seasonal contrast is much less pronounced. However, Keskinen and Huba (1990) found that high-latitude plasma irregularities should transition to a fully collisional regime around scales of 2-3 km, meaning there could be multiple scale-dependent regimes in the observable plasma diffusion in the polar caps, with diffusion primarily being observed on scales smaller than a threshold. Moreover, simultaneous growth might impact structure lifetimes, a topic that was explored recently in a paper by Lamarche et al. (2020). We believe more careful attention to growth, in addition to the use of higher resolution plasma density data, is necessary to further our knowledge about ionospheric plasma structure lifetimes. In addition, the analysis presented here is sensitive to the assumed polar cap convection velocity. In future investigations of plasma structure lifetimes, special care should be taken in treating plasma convection velocity, e.g. by using methods of observing plasma drift velocity (Park et al., 2015).

5 Conclusion

In this study we have approached the subject of field-perpendicular plasma diffusion and field-perpendicular plasma structure lifetimes from two angles. By using almost 5 years of in-situ data from Swarm A, and by applying ionospheric models, we have made several new observations regarding structure lifetimes, decay time, and their seasonal dependencies. Both the in-situ data and the ionospheric models support the claim that perpendicular diffusion in the F-region polar caps is highly dependent on the relationship between E- and F-region conductances.

Our results indicate that we are able to observe the characteristics of local summer diffusion in both the northern and southern polar caps. This leads to, for the first time as far the authors are aware, a systematic prediction of small-scale structure life-

times in the F-region polar caps. We find that for the smallest scale investigated, which corresponds to frequencies between 6.6 Hz and 8 Hz, with a scale length of 1 km, structure lifetimes range from 1 hour during local summer to around 3 hours approaching local winter. Although the seasonal contrast in plasma structure time harmonizes with reported seasonal dependencies in polar cap plasma irregularities, more work is needed to estimate plasma structure times more accurately, e.g. by using higher resolution plasma density data. There is a large discrepancy in the theoretical scale-dependency of decay time due to plasma diffusion and the in-situ-estimated structure lifetimes, and future investigations into the matter is called for.

Acknowledgments

This work is a part of the 4DSpace initiative at the University of Oslo, and is supported in part by Research Council of Norway grants 275655, 275653 and 267408. The authors acknowledge ESA for the provision of the Swarm data, which was accessed from `https://earth.esa.int/web/guest/swarm/data-access`, and NASA/GSFC's Space Physics Data Facility's OMNIWeb service. The authors would like to extend thanks to D. J. Knudsen, J. K. Burchill, and S. C. Buchert for their work on the Swarm Thermal ion imager instrument, and the authors are grateful to I. Ivarsen for proofreading. Finally, the authors would also like to extend their warmest gratitude towards the reviewers who made extraordinarily thoughtful, constructive, and thorough reviews of this study.

References

Basu, S., MacKenzie, E., & Basu, S. (1988, May). Ionospheric constraints on VHF/UHF communications links during solar maximum and minimum periods. *Radio Science*, *23*(3), 363–378. Retrieved 2018-09-02, from `https://agupubs.onlinelibrary.wiley.com/doi/abs/10.1029/RS023i003p00363` doi: 10.1029/RS023i003p00363

Bilitza, D., Altadill, D., Zhang, Y., Mertens, C., Truhlik, V., Richards, P., ... Reinisch, B. (2014). The International Reference Ionosphere 2012 a model of international collaboration. *Journal of Space Weather and Space Climate*, *4*, A07. Retrieved 2018-06-13, from `https://www.swsc-journal.org/articles/swsc/abs/2014/01/swsc130043/swsc130043.html` doi: 10.1051/swsc/2014004

Bilitza, D., & Reinisch, B. W. (2008, August). International Reference Ionosphere 2007: Improvements and new parameters. *Advances in Space Research*, *42*(4), 599–609. Retrieved 2018-06-13, from `http://www.sciencedirect.com/science/article/pii/S0273117708000288` doi: 10.1016/j.asr.2007.07.048

Braginskii, S. I. (1965). Transport Processes in a Plasma. *Reviews of Plasma Physics*, *1*, 205. Retrieved 2020-02-27, from `http://adsabs.harvard.edu/abs/1965RvPP....1..205B`

Chartier, A. T., Mitchell, C. N., & Miller, E. S. (2018, March). Annual Occurrence Rates of Ionospheric Polar Cap Patches Observed Using Swarm. *Journal of Geophysical Research: Space Physics*, *123*(3), 2327–2335. Retrieved 2018-11-11, from `https://agupubs.onlinelibrary.wiley.com/doi/abs/10.1002/2017JA024811` doi: 10.1002/2017JA024811

Coley, W. R., & Heelis, R. A. (1998, February). Structure and occurrence of polar ionization patches. *Journal of Geophysical Research: Space Physics*, *103*(A2), 2201–2208. Retrieved 2018-09-06, from `https://agupubs.onlinelibrary.wiley.com/doi/abs/10.1029/97JA03345` doi: 10.1029/97JA03345

Cowley, S. W. H. (2000). TUTORIAL: Magnetosphere-Ionosphere Interactions: A Tutorial Review. *Washington DC American Geophysical Union Geophysical Monograph Series*, *118*, 91. Retrieved 2018-03-07, from `http://adsabs.harvard.edu/abs/2000GMS...118...91C` doi:

10.1029/GM118p0091

Cowley, S. W. H., & Lockwood, M. (1992, February). Excitation and decay of solar wind-driven flows in the magnetosphere-ionosphere system. *Annales Geophysicae*, *10*, 103–115. Retrieved 2018-03-07, from http://adsabs.harvard.edu/abs/1992AnGeo..10..103C

Danskin, D. W., Koustov, A. V., Ogawa, T., Nishitani, N., Nozawa, S., Milan, S. E., ... Andre, D. (2002, September). On the factors controlling occurrence of F-region coherent echoes. *Annales Geophysicae*, *20*(9), 1385–1397. Retrieved 2019-02-18, from https://www.ann-geophys.net/20/1385/2002/ doi: https://doi.org/10.5194/angeo-20-1385-2002

Dungey, J. W. (1961, January). Interplanetary Magnetic Field and the Auroral Zones. *Physical Review Letters*, *6*, 47–48. Retrieved 2018-03-08, from http://adsabs.harvard.edu/abs/1961PhRvL...6...47D doi: 10.1103/PhysRevLett.6.47

Foster, J. C. (1984, February). Ionospheric signatures of magnetospheric convection. *Journal of Geophysical Research: Space Physics*, *89*(A2), 855–865. Retrieved 2018-09-06, from https://agupubs.onlinelibrary.wiley.com/doi/abs/10.1029/JA089iA02p00855 doi: 10.1029/JA089iA02p00855

Friis-Christensen, E., Lhr, H., & Hulot, G. (2006, April). Swarm: A constellation to study the Earths magnetic field. *Earth, Planets and Space*, *58*, BF03351933. doi: 10.1186/BF03351933

Ghezelbash, M., Koustov, A. V., Themens, D. R., & Jayachandran, P. T. (2014, December). Seasonal and diurnal variations of PolarDARN F region echo occurrence in the polar cap and their causes. *Journal of Geophysical Research: Space Physics*, *119*(12), 10,426–10,439. Retrieved 2018-09-03, from https://agupubs.onlinelibrary.wiley.com/doi/abs/10.1002/2014JA020726 doi: 10.1002/2014JA020726

Grant, I. F., MacDougall, J. W., Ruohoniemi, J. M., Bristow, W. A., Sofko, G. J., Koehler, J. A., ... Andr, D. (1995). Comparison of plasma flow velocities determined by the ionosonde Doppler drift technique, SuperDARN radars, and patch motion. *Radio Science*, *30*(5), 1537–1549. Retrieved 2020-02-24, from https://agupubs.onlinelibrary.wiley.com/doi/abs/10.1029/95RS00831 doi: 10.1029/95RS00831

Grocott, A., Badman, S. V., Cowley, S. W. H., Yeoman, T. K., & Cripps, P. J. (2004, April). The influence of IMF By on the nature of the nightside high-latitude ionospheric flow during intervals of positive IMF Bz. *Annales Geophysicae*, *22*(5), 1755–1764. Retrieved 2020-07-16, from https://angeo.copernicus.org/articles/22/1755/2004/ (Publisher: Copernicus GmbH) doi: https://doi.org/10.5194/angeo-22-1755-2004

Heppner, J. P., Liebrecht, M. C., Maynard, N. C., & Pfaff, R. F. (1993, February). High-latitude distributions of plasma waves and spatial irregularities from DE 2 alternating current electric field observations. *Journal of Geophysical Research: Space Physics*, *98*(A2), 1629–1652. Retrieved 2018-09-06, from https://agupubs.onlinelibrary.wiley.com/doi/abs/10.1029/92JA01836 doi: 10.1029/92JA01836

Hosokawa, K., Moen, J. I., Shiokawa, K., & Otsuka, Y. (2011). Decay of polar cap patch. *Journal of Geophysical Research: Space Physics*, *116*(A5). Retrieved 2020-11-01, from https://agupubs.onlinelibrary.wiley.com/doi/abs/10.1029/2010JA016297 (_eprint: https://agupubs.onlinelibrary.wiley.com/doi/pdf/10.1029/2010JA016297) doi: 10.1029/2010JA016297

Huba, J. D., & Ossakow, S. L. (1981). Diffusion of small-scale density irregularities during equatorial spread F. *Journal of Geophysical Research: Space Physics*, *86*(A11), 9107–9114. Retrieved 2020-02-17, from https://agupubs.onlinelibrary.wiley.com/doi/abs/10.1029/JA086iA11p09107

doi: 10.1029/JA086iA11p09107

Ivarsen, M. F., Jin, Y., Spicher, A., & Clausen, L. B. N. (2019). Direct Evidence for the Dissipation of Small-Scale Ionospheric Plasma Structures by a Conductive E Region. *Journal of Geophysical Research: Space Physics*, *124*(4), 2935–2942. Retrieved 2019-09-12, from https://agupubs.onlinelibrary.wiley.com/doi/abs/10.1029/2019JA026500 doi: 10.1029/2019JA026500

Jin, Y., Miloch, W. J., Moen, J. I., & Clausen, L. B. N. (2018). Solar cycle and seasonal variations of the GPS phase scintillation at high latitudes. *Journal of Space Weather and Space Climate*, *8*, A48. Retrieved 2018-11-22, from https:/articles/swsc/abs/2018/01/swsc170089/swsc170089.html doi: 10.1051/swsc/2018034

Jin, Y., Moen, J. I., Oksavik, K., Spicher, A., Clausen, L. B. N., & Miloch, W. J. (2017). GPS scintillations associated with cusp dynamics and polar cap patches. *Journal of Space Weather and Space Climate*, *7*, A23. Retrieved 2018-09-14, from https://www.swsc-journal.org/articles/swsc/abs/2017/01/swsc170040/swsc170040.html doi: 10.1051/swsc/2017022

Jin, Y., Spicher, A., Xiong, C., Clausen, L. B. N., Kervalishvili, G., Stolle, C., & Miloch, W. J. (2019). Ionospheric Plasma Irregularities Characterized by the Swarm Satellites: Statistics at High Latitudes. *Journal of Geophysical Research: Space Physics*, *124*(2), 1262–1282. Retrieved 2020-01-20, from https://agupubs.onlinelibrary.wiley.com/doi/abs/10.1029/2018JA026063 doi: 10.1029/2018JA026063

Johnsen, R., & Biondi, M. A. (1980). Laboratory measurements of the O+(D) + N2 and O+(D) + O2 reaction rate coefficients and their ionospheric implications. *Geophysical Research Letters*, *7*(5), 401–403. Retrieved 2020-07-18, from https://agupubs.onlinelibrary.wiley.com/doi/abs/10.1029/GL007i005p00401 (_eprint: https://agupubs.onlinelibrary.wiley.com/doi/pdf/10.1029/GL007i005p00401) doi: 10.1029/GL007i005p00401

Kelley, M. C., Vickrey, J. F., Carlson, C. W., & Torbert, R. (1982, June). On the origin and spatial extent of high-latitude F region irregularities. *Journal of Geophysical Research: Space Physics*, *87*(A6), 4469–4475. Retrieved 2018-09-03, from https://agupubs.onlinelibrary.wiley.com/doi/abs/10.1029/JA087iA06p04469 doi: 10.1029/JA087iA06p04469

Keskinen, M. J., & Huba, J. D. (1990, September). Nonlinear evolution of high-latitude ionospheric interchange instabilities with scale-size-dependent magnetospheric coupling. *Journal of Geophysical Research: Space Physics*, *95*(A9), 15157–15166. Retrieved 2018-03-05, from http://onlinelibrary.wiley.com/doi/10.1029/JA095iA09p15157/abstract doi: 10.1029/JA095iA09p15157

King, J. H., & Papitashvili, N. E. (2005). Solar wind spatial scales in and comparisons of hourly Wind and ACE plasma and magnetic field data. *Journal of Geophysical Research: Space Physics*, *110*(A2). Retrieved 2020-07-16, from https://agupubs.onlinelibrary.wiley.com/doi/abs/10.1029/2004JA010649 (_eprint: https://agupubs.onlinelibrary.wiley.com/doi/pdf/10.1029/2004JA010649) doi: 10.1029/2004JA010649

Kivanc, , & Heelis, R. A. (1998, April). Spatial distribution of ionospheric plasma and field structures in the high-latitude F region. *Journal of Geophysical Research*, *103*, 6955–6968. Retrieved 2018-08-13, from http://adsabs.harvard.edu/abs/1998JGR...103.6955K doi: 10.1029/97JA03237

Knudsen, D. J., Burchill, J. K., Buchert, S. C., Eriksson, A. I., Gill, R., Wahlund, J.-E., ... Moffat, B. (2017, February). Thermal ion imagers and Langmuir probes in the Swarm electric field instruments. *Journal of Geophysical Research: Space Physics*, *122*(2), 2016JA022571. Retrieved 2018-03-07, from http://onlinelibrary.wiley.com/doi/10.1002/2016JA022571/abstract

doi: 10.1002/2016JA022571

Lamarche, L. J., Varney, R. H., & Siefring, C. L. (2020). Analysis of Plasma Irregularities on a Range of Scintillation-Scales Using the Resolute Bay Incoherent Scatter Radars. *Journal of Geophysical Research: Space Physics*, *125*(3), e2019JA027112. Retrieved 2020-12-15, from https://agupubs.onlinelibrary.wiley.com/doi/abs/10.1029/2019JA027112 (_eprint: https://agupubs.onlinelibrary.wiley.com/doi/pdf/10.1029/2019JA027112) doi: https://doi.org/10.1029/2019JA027112

Lotko, W., Smith, R. H., Zhang, B., Ouellette, J. E., Brambles, O. J., & Lyon, J. G. (2014, July). Ionospheric control of magnetotail reconnection. *Science*, *345*(6193), 184–187. Retrieved 2020-04-07, from https://science.sciencemag.org/content/345/6193/184 (Publisher: American Association for the Advancement of Science Section: Report) doi: 10.1126/science.1252907

Milan, S. E., Davies, J. A., & Lester, M. (1999). Coherent HF radar backscatter characteristics associated with auroral forms identified by incoherent radar techniques: a comparison of CUTLASS and EISCAT observations. *Journal of Geophysical Research: Space Physics*, *104*(A10), 22591–22604.

Moisan, M., & Pelletier, J. (2012). Hydrodynamic Description of a Plasma. In M. Moisan & J. Pelletier (Eds.), *Physics of Collisional Plasmas: Introduction to High-Frequency Discharges* (pp. 203–335). Dordrecht: Springer Netherlands. Retrieved 2019-09-02, from https://doi.org/10.1007/978-94-007-4558-2_3 doi: 10.1007/978-94-007-4558-2_3

Noja, M., Stolle, C., Park, J., & Lhr, H. (2013, May). Long-term analysis of ionospheric polar patches based on CHAMP TEC data. *Radio Science*, *48*(3), 289–301. Retrieved 2018-09-07, from https://agupubs.onlinelibrary.wiley.com/doi/abs/10.1002/rds.20033 doi: 10.1002/rds.20033

Park, J., Lhr, H., Stolle, C., Malhotra, G., B. H. Baker, J., Buchert, S., & Gill, R. (2015, July). Estimating along-track plasma drift speed from electron density measurements by the three Swarm satellites. *Annales Geophysicae*, *33*, 829–835. doi: 10.5194/angeo-33-829-2015

Picone, J. M., Hedin, A. E., Drob, D. P., & Aikin, A. C. (2002). NRLMSISE-00 empirical model of the atmosphere: Statistical comparisons and scientific issues. *Journal of Geophysical Research: Space Physics*, *107*(A12), SIA 15–1–SIA 15–16. Retrieved 2019-09-02, from https://agupubs.onlinelibrary.wiley.com/doi/abs/10.1029/2002JA009430 doi: 10.1029/2002JA009430

Prikryl, P., Jayachandran, P. T., Chadwick, R., & Kelly, T. D. (2015, May). Climatology of GPS phase scintillation at northern high latitudes for the period from 2008 to 2013. *Ann. Geophys.*, *33*(5), 531–545. Retrieved 2018-09-13, from https://www.ann-geophys.net/33/531/2015/ doi: 10.5194/angeo-33-531-2015

Reiff, P. H., & Burch, J. L. (1985). IMF By-dependent plasma flow and Birkeland currents in the dayside magnetosphere: 2. A global model for northward and southward IMF. *Journal of Geophysical Research: Space Physics*, *90*(A2), 1595–1609. Retrieved 2020-11-01, from https://agupubs.onlinelibrary.wiley.com/doi/abs/10.1029/JA090iA02p01595 (_eprint: https://agupubs.onlinelibrary.wiley.com/doi/pdf/10.1029/JA090iA02p01595) doi: 10.1029/JA090iA02p01595

Schunk, R. W., & Nagy, A. F. (1980). Ionospheres of the terrestrial planets. *Reviews of Geophysics*, *18*(4), 813–852. Retrieved 2019-09-02, from https://agupubs.onlinelibrary.wiley.com/doi/abs/10.1029/RG018i004p00813 doi: 10.1029/RG018i004p00813

Schunk, R. W., & Sojka, J. J. (1987, November). A theoretical study of the lifetime and transport of large ionospheric density structures. *Journal of Geophysical Research: Space Physics*, *92*(A11), 12343–12351. Retrieved 2018-09-

06, from https://agupubs.onlinelibrary.wiley.com/doi/abs/10.1029/JA092iA11p12343 doi: 10.1029/JA092iA11p12343

Spicher, A., Clausen, L. B. N., Miloch, W. J., Lofstad, V., Jin, Y., & Moen, J. I. (2017, March). Interhemispheric study of polar cap patch occurrence based on Swarm in situ data. *Journal of Geophysical Research: Space Physics*, *122*(3), 3837–3851. Retrieved 2018-09-07, from https://agupubs.onlinelibrary.wiley.com/doi/abs/10.1002/2016JA023750 doi: 10.1002/2016JA023750

Thomas, E. G., Hosokawa, K., Sakai, J., Baker, J. B. H., Ruohoniemi, J. M., Taguchi, S., ... McWilliams, K. A. (2015). Multi-instrument, high-resolution imaging of polar cap patch transportation. *Radio Science*, *50*(9), 904–915. Retrieved 2020-02-24, from https://agupubs.onlinelibrary.wiley.com/doi/abs/10.1002/2015RS005672 doi: 10.1002/2015RS005672

Thbault, E., Finlay, C. C., Beggan, C. D., Alken, P., Aubert, J., Barrois, O., ... Zvereva, T. (2015, May). International Geomagnetic Reference Field: the 12th generation. *Earth, Planets and Space*, *67*(1), 79. Retrieved 2019-09-02, from https://doi.org/10.1186/s40623-015-0228-9 doi: 10.1186/s40623-015-0228-9

Trbs, M., & Heinzel, G. (2006, February). Improved spectrum estimation from digitized time series on a logarithmic frequency axis. *Measurement*, *39*(2), 120–129. Retrieved 2018-03-06, from http://www.sciencedirect.com/science/article/pii/S026322410500117X doi: 10.1016/j.measurement.2005.10.010

Tsunoda, R. T. (1988, November). High-latitude F region irregularities: A review and synthesis. *Reviews of Geophysics*, *26*(4), 719–760. Retrieved 2018-03-07, from http://onlinelibrary.wiley.com/doi/10.1029/RG026i004p00719/abstract doi: 10.1029/RG026i004p00719

Vickrey, J. F., & Kelley, M. C. (1982, June). The effects of a conducting E layer on classical F region cross-field plasma diffusion. *Journal of Geophysical Research: Space Physics*, *87*(A6), 4461–4468. Retrieved 2018-03-06, from http://onlinelibrary.wiley.com/doi/10.1029/JA087iA06p04461/abstract doi: 10.1029/JA087iA06p04461

Welch, P. (1967, June). The use of fast Fourier transform for the estimation of power spectra: A method based on time averaging over short, modified periodograms. *IEEE Transactions on Audio and Electroacoustics*, *15*(2), 70–73. doi: 10.1109/TAU.1967.1161901

Wood, A. G., & Pryse, S. E. (2010, July). Seasonal influence on polar cap patches in the high-latitude nightside ionosphere. *Journal of Geophysical Research: Space Physics*, *115*(A7). Retrieved 2018-09-03, from https://agupubs.onlinelibrary.wiley.com/doi/abs/10.1029/2009JA014985 doi: 10.1029/2009JA014985